Lu *et al. J Mater Inf* 2024;4:31
DOI: 10.20517/jmi.2024.65

Journal of Materials Informatics

Research Article

Open Access

Check for updates

N-heterocyclic carbene coordinated single atom catalysts on C_2N for enhanced nitrogen reduction

Wenming Lu[#], Dian Zheng[#], Daifei Ye, Jiasheng Peng, Xiaxia Gong, Jing Xu, Wei Liu[*]

Department of Optical Engineering, College of Optical, Mechanical and Electrical Engineering, Zhejiang A&F University, Hangzhou 311300, Zhejiang, China.
[#]Authors contributed equally.

[*]**Correspondence to:** Prof. Wei Liu, Department of Optical Engineering, College of Optical, Mechanical and Electrical Engineering, Zhejiang A&F University, No. 666, Wusu Street, Lin'an District, Hangzhou 311300, Zhejiang, China, E-mail: weiliu@zafu.edu.cn

How to cite this article: Lu W, Zheng D, Ye D, Peng J, Gong X, Xu J, Liu W. N-heterocyclic carbene coordinated single atom catalysts on C_2N for enhanced nitrogen reduction. *J Mater Inf* 2024;4:31. https://dx.doi.org/10.20517/jmi.2024.65

Received: 28 Oct 2024 **First Decision:** 25 Nov 2024 **Revised:** 6 Dec 2024 **Accepted:** 14 Dec 2024 **Published:** 28 Dec 2024

Academic Editor: Ming Hu **Copy Editor:** Ping Zhang **Production Editor:** Ping Zhang

Abstract

Single-atom catalysts (SACs) with N-heterocyclic carbene (NHC) coordination provide an effective strategy for enhancing nitrogen reduction reaction (NRR) performance by modulating the electronic properties of the metal active sites. In this work, we designed a novel NHC-coordinated SAC by embedding transition metals (TM) into a two-dimensional C_2N-based nanomaterial (TM@C_2N-NCM) and evaluated the NRR catalytic performance using a combination of density functional theory and machine learning. A multi-step screening identified eight high-performance catalysts (TM = Nb, Fe, Mn, W, V, Ta, Zr, Ti), with Nb@C_2N-NCM showing the best performance (limiting potential = -0.29 V). All catalysts demonstrated lower limiting potential values compared to their TM@graphene-NCM counterparts, revealing the effectiveness of the C_2N substrate in enhancing catalytic activity. Machine learning analysis achieved high predictive accuracy (coefficient of determination = 0.91; mean absolute error = 0.19) and identified final step protonation (S_6), Mendeleev number (N_m), and d-electron count (N_d) as key factors influencing catalytic performance. This study offers valuable insights into the rational design of NHC-coordinated SACs and highlights the potential of C_2N-based nanomaterials for advancing high-performance NRR electrocatalysts.

Keywords: Nitrogen reduction reaction, single-atom catalysts, N-heterocyclic carbenes, C_2N, machine learning

INTRODUCTION

Ammonia (NH_3) is indispensable in modern industry, primarily as an essential component in global fertilizer production and as a key precursor in the synthesis of numerous chemicals[1]. Moreover, NH_3 has gained increased attention as a promising carbon-free energy carrier due to its high hydrogen content (17.6 wt%) and substantial energy density (4.3 kWh/kg)[2,3]. This dual role underscores the growing need for sustainable and efficient NH_3 production methods[4,5]. However, the industrial synthesis of NH_3 is dominated by the Haber-Bosch process, which operates under extreme conditions (~500 °C, 200-300 atm), accounting for approximately 2% of global energy consumption and significant greenhouse gas emissions[6-8]. The electrocatalytic nitrogen reduction reaction (NRR) offers a promising green alternative, enabling NH_3 synthesis under mild conditions with significantly reduced energy consumption and zero carbon emissions[9-14]. Nevertheless, the NRR process still faces challenges such as low activity and poor selectivity, which severely limits their practical applicability[15,16]. Therefore, developing catalysts with high activity and selectivity is crucial for enhancing NRR performance and advancing sustainable NH_3 synthesis.

Single-atom catalysts (SACs), characterized by atomically dispersed metal atoms on a substrate, have emerged as a promising class of catalysts due to their maximized metal atom utilization, tunable electronic properties, and exceptional catalytic performance[17-24]. SACs have shown great promise in various energy conversion reactions[25-27], and numerous high-performance SACs for NRR have been reported both experimentally and theoretically[28-35]. For instance, Feng *et al.* synthesized an efficient NRR electrocatalyst by immobilizing Ru atoms onto a graphdiyne/graphene sandwich structure, achieving a high NH_3 yield rate of 56.8 μg h^{-1} mg_{cat}^{-1} and a Faradaic efficiency (FE) of 37.6%[36]. Similarly, Geng *et al.* developed a nitrogen-doped graphene-based Ru SAC (Ru SAs/N-C) with an FE of 29.6% and an impressive NH_3 yield rate of 120.9 μg h^{-1} mg_{cat}^{-1}, which is nearly one order of magnitude higher than previously reported values[37]. Ling *et al.* conducted high-throughput screening of nitrogen-doped graphene-based SACs for NRR, revealing the catalytic potential of different transition metals (TMs) (3d, 4d, 5d) in various coordination environments (TM-N_xC_y). Among these, W_1C_3 exhibited the best performance, with a remarkably low onset potential of 0.25 V[38]. These studies demonstrate that catalytic performance can be effectively tuned by modulating the types of metal atoms, substrates, and the local coordination environment around the active sites. A critical factor in achieving an outstanding NRR catalyst is the optimal synergy between the metal atom and the substrate. On the one hand, strong metal-substrate interactions are essential to stabilize the isolated metal atoms and prevent their aggregation[39,40]. On the other hand, the inherent properties of the metal atom, such as its electronic configuration and *d*-orbital occupation, play a key role in determining its reactivity[41,42]. Simultaneously, the local coordination environment provided by the substrate modulates the electronic structure of the metal, affecting its ability to activate N_2 and promote selective catalytic pathways[43,44]. This delicate balance between metal atom characteristics and substrate interactions is essential to enhancing overall catalytic performance.

N-heterocyclic carbene nanomaterials (NCMs), which incorporate molecular N-heterocyclic carbenes (NHCs) into the lattices of low-dimensional carbon materials, represent a novel class of carbon-nitride materials with well-defined porous structures formed by NHC units[45-49]. These materials combine the advantages of NHCs and the rigid, periodic carbon frameworks, facilitating the formation of robust C-TM bonds with metal atoms. Simultaneously, the σ-donating and π-accepting properties of NHCs interact with the *d*-orbitals of the metal, modulating its electronic structure and thereby enhancing catalytic activity[47,49]. Thus, NCMs offer a distinctive NHC coordination environment, making them highly promising platforms for the design of high-performance SACs. In our previous work, graphene-based NCMs have been successfully employed to anchor various TMs (TM@graphene-NCM), demonstrating significant catalytic potential for NRR[45,47]. Among them, a Mn-embedded SAC exhibited remarkable performance, achieving a

limiting potential (U_L) as low as -0.51 V[47].

C_2N-*h*2D (C_2N), a two-dimensional porous carbon nitride material first synthesized in 2015, has garnered attention as an excellent substrate for anchoring metal atoms due to its wide band gap, high electron mobility, and excellent thermal stability[50,51]. Its unique structure, characterized by electron-rich nitrogen atoms exposed within a two-dimensional framework, offers an ideal platform for NHC functionalization, facilitating the design of novel NCM. Unlike graphene, C_2N possesses distinct structural and electronic properties, providing a different local coordination environment that modulates the electronic properties of the anchored metal atoms, potentially enhancing their catalytic performance[24,52,53]. Inspired by these advantages, we systematically investigated C_2N-based NCMs as platforms for SACs and explored their potential in NRR catalysis.

In this study, we designed 28 SACs by embedding 3d, 4d, and 5d TMs into a C_2N-based NCM system, denoted as TM@C_2N-NCM. Using a combination of first-principles calculations and machine learning (ML), we systematically evaluated the NRR catalytic performance of these SACs. Through a multiple-step screening process, eight candidates with high catalytic activity and selectivity for NRR were identified, all exhibiting lower U_L than their TM@Graphene-NCM counterparts, demonstrating enhanced catalytic performance. Notably, Nb@C_2N-NCM showed the best performance, with a U_L of -0.29 V. ML models further revealed the intrinsic factors governing the varied NRR performance across different SACs. Compared to graphene-based NCMs, the introduction of C_2N not only improved catalytic activity but also expanded the range of TMs that could be utilized as promising SACs for NRR. This study provides valuable insights into the design of highly efficient NRR electrocatalysts and offers strategies for developing more effective SACs in future research.

MATERIALS AND METHODS

All density functional theory (DFT) calculations were carried out using the Vienna Ab Initio Simulation Package (VASP)[54], with the electronic interactions between ions and electrons described through the projector augmented wave (PAW) method[55]. The exchange-correlation effects were treated using the generalized gradient approximation (GGA) combined with the Perdew-Burke-Ernzerhof (PBE) functionals[56]. For the plane-wave basis set, a kinetic energy cutoff of 500 eV was chosen to ensure computational accuracy. The energy convergence criterion was set at 10^{-5} eV, while the force convergence threshold was fixed at 0.01 eV/Å. The Brillouin zone was sampled using 2 × 2 × 1 and 8 × 8 × 1 Gamma-centered k-points for geometry optimizations and electronic property calculations[57]. Spin polarization was included in all calculations to account for potential magnetic effects. A vacuum layer of 18 Å along the Z-direction was applied to eliminate spurious interactions between periodic images. The thermal stability of the catalysts was evaluated using ab initio molecular dynamics (AIMD) simulations within the canonical (NVT) ensemble. A Nosé thermostat was applied to maintain the temperature at 500 K, with a time step of 1 fs over a simulation period of 10 ps[58]. To incorporate van der Waals forces between NRR intermediates and the catalyst, we employed the DFT-D3 method for calculating free energy and electronic structure[59]. Charge transfer was analyzed through Bader charge calculations[60]. Detailed methods for evaluating adsorption energies (E_{ads}), Gibbs free energy changes (ΔG), and differential charge density are provided in the Supplementary Materials.

For the ML analysis, we utilized three non-linear regression algorithms: Random Forest Regression (RFR), Gradient Boosting Regression (GBR), and Extreme GBR (XGBR)[61-65]. A grid search technique was applied to optimize the hyperparameters for each model[66,67]. These algorithms were selected for their robustness against overfitting, their ability to process high-dimensional datasets, and their superior predictive accuracy

in material property modeling. All ML models were implemented using the Scikit-learn library[68]. To prevent overfitting, data normalization was performed prior to training, and a 5-fold cross-validation was used to validate model performance. Model accuracy was evaluated using the coefficient of determination (R^2) and mean absolute error (MAE), with ideal models approaching an R^2 value of 1 and an MAE close to 0. For feature selection, we applied both Pearson correlation coefficient heatmap analysis and Recursive Feature Elimination (RFE)[69]. The heatmap identifies highly correlated features, enabling us to eliminate redundancy, while RFE iteratively removes the least important features, further refining the feature set. By combining these two methods, we derived the optimal feature subset for input into the ML models. To interpret the ML results and understand the influence of key descriptors on catalytic activity, the Shapley Additive Explanations (SHAP) method was employed. SHAP provides the magnitude and direction of the contribution of each feature to the model predictions[70]. In the SHAP summary plot, each point corresponds to a sample, with the horizontal axis showing the SHAP value, indicating the impact of the feature on the prediction. Positive SHAP values contribute to an increase in the predicted value, while negative values result in a decrease. The color of each point reflects the feature value, with red indicating higher values and blue representing lower values.

RESULTS AND DISCUSSION

Structure of TM@C_2N-NCM

To construct the target catalysts, a C_2N-based NCM was designed by introducing three classic five-membered NHC units into a 2 × 2 C_2N supercell. TM atoms from the 3d, 4d, and 5d series were subsequently anchored into the pores of the C_2N-based NCM framework, resulting in the TM@C_2N-NCM structure (see Figure 1A). The lattice constant is a = b = 16.63 Å. The TMs studied include 3d (Sc, Ti, V, Cr, Mn, Fe, Co, Ni, Cu, Zn), 4d (Y, Zr, Nb, Mo, Ru, Rh, Pd, Ag, Cd), and 5d (Hf, Ta, W, Re, Os, Ir, Pt, Au, Hg) elements [Figure 1B]. To gain a more comprehensive understanding of the role of the substrate and various metals and identify broader trends, toxic Cd and Hg were also included in the study. Each TM atom is stably coordinated by three NHC units, forming robust TM-C bonds. Due to the presence of three five-membered rings, the non-planar TM@C_2N-NCM structures result in the exposure of these metal centers on the surface, which is beneficial for N_2 adsorption and catalytic activity.

To evaluate the stability of the metal atoms on the substrate, the binding energies (E_b) of the TMs with the C_2N-NCM were calculated. As shown in Figure 1C, all TMs exhibited negative E_b, except for Au, which had a slightly positive value of 0.02 eV, indicating weak interaction between Au and the substrate. For the remaining 27 TMs, the E_b values range from -10.03 eV (Os) to -0.75 eV (Hg). These negative values confirm their stable adsorption on the C_2N-NCM substrate, with more negative values indicating stronger metal-substrate interactions. Additionally, we found that the trend in E_b is strongly influenced by the d-electron configuration of the TMs, which is consistent with observations from TM@graphene-NCM. Metals located in the middle of each period (e.g., Fe, Ru, Os) exhibited more negative E_b values, which can be attributed to a balanced electron donation from the metal to the NHC ligands and back-donation from the NHCs to the *d*-orbitals of metal atoms. Early TMs (e.g., Ti, Zr, Ta) lack sufficient *d*-electrons for effective back-donation, while late TMs (e.g., Zn, Cd, Hg) have fewer vacant *d*-orbitals to accept electron donation from the NHCs. To further verify the thermodynamic stability of the catalysts, AIMD simulations were performed. Nb@C_2N-NCM, which later demonstrated the best catalytic performance, was selected as a representative example to further verify its stability. The results showed that the energy fluctuations remained near equilibrium throughout the simulation, with the Nb atom firmly anchored in the NHC coordination environment, confirming the favorable thermodynamic stability of the structure (see Supplementary Figure 1). Based on these results, 27 SACs (excluding Au) were identified as stable candidates for further catalytic investigation.

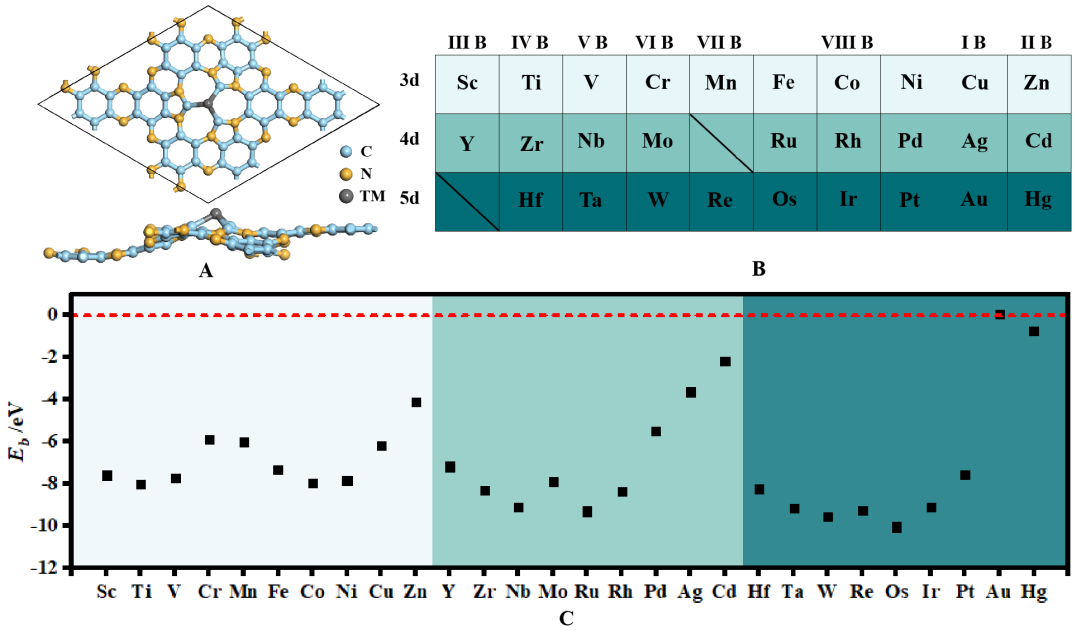

Figure 1. (A) Top and side views of the optimized structure of TM@C_2N-NCM. TM, C, and N atoms are represented in grey, yellow, and blue, respectively; (B) The 3d, 4d, and 5d transition metals selected for this study; (C) Calculated binding energies (E_b) of the TMs on the C_2N-NCM substrate. TM@C_2N-NCM:Transition metals into a two-dimensional C_2N-based nanomaterial; TM: Transition metals.

Screening strategy

As shown in Figure 2, the NRR proceeds through several mechanistic pathways, including Distal, Alternating, Enzymatic, and Consecutive routes, each involving different proton and electron transfer sequences. Given this complexity, a systematic and efficient screening approach is essential for evaluating the catalytic performance of the designed catalysts. A three-step screening strategy was developed based on previous theoretical studies[38,71,72]. The first criterion is the E_{ads} of N_2, as effective N_2 binding is crucial for initiating NRR. A threshold of E_{ads} < -0.50 eV was established to ensure strong chemisorption. Although the pathways differ in intermediates, two protonation steps are critical across all mechanisms: the first protonation ($*N_2 + H^+ + e^- = *NNH$), which breaks the N≡N triple bond, and the last protonation step ($*NH_2 + H^+ + e^- = *NH_3$), where nitrogen transitions from a half-filled sp^3 hybrid orbital in $*NH_2$ to a fully filled sp^3 configuration in NH_3. These two steps have been widely recognized in previous studies as the most likely potential-determining steps (PDS) in NRR, primarily due to the significant energy barriers associated with them[73-77]. Thus, the second and third criteria focus on the ΔG for these protonation steps, with ΔG < 0.55 eV as the criterion for efficient catalysis. By applying these three criteria, i.e., favorable N_2 adsorption and ΔG for the first and last protonation steps, we systematically screened 27 SACs, identifying the most promising candidates for efficient NRR in the following.

N_2 adsorption and activation

The adsorption of N_2 on TM@C_2N-NCM occurs in two primary configurations, i.e., end-on and side-on. The corresponding E_{ads} and N-N bond lengths for both configurations are summarized in Figure 3, with detailed values provided in Supplementary Table 1. Among the 27 investigated TMs, Zn, Ru, Cd, and Hg can only stabilize N_2 in the end-on configuration, while the remaining metals can accommodate both adsorption modes. The E_{ads} values for the end-on configuration range from -1.35 eV to -0.15 eV, while those for the side-on configuration range from -1.44 eV to -0.19 eV. More negative E_{ads} values indicate stronger N_2 binding, suggesting that the N_2 molecule preferentially adopts the end-on configuration for most TMs. The N-N bond lengths after adsorption vary between 1.10 Å and 1.19 Å, indicative of varying degrees of N_2

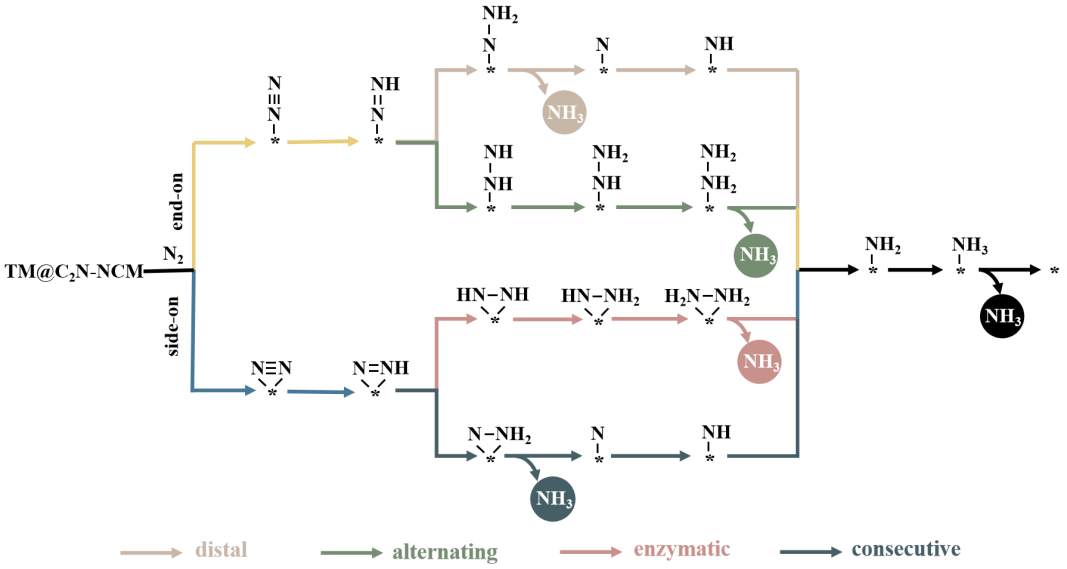

Figure 2. Distal, alternating, enzymatic and consecutive reaction pathways for NRR. NRR: Nitrogen reduction reaction; TM@C_2N-NCM:Transition metals into a two-dimensional C_2N-based nanomaterial; NH_3: Ammonia.

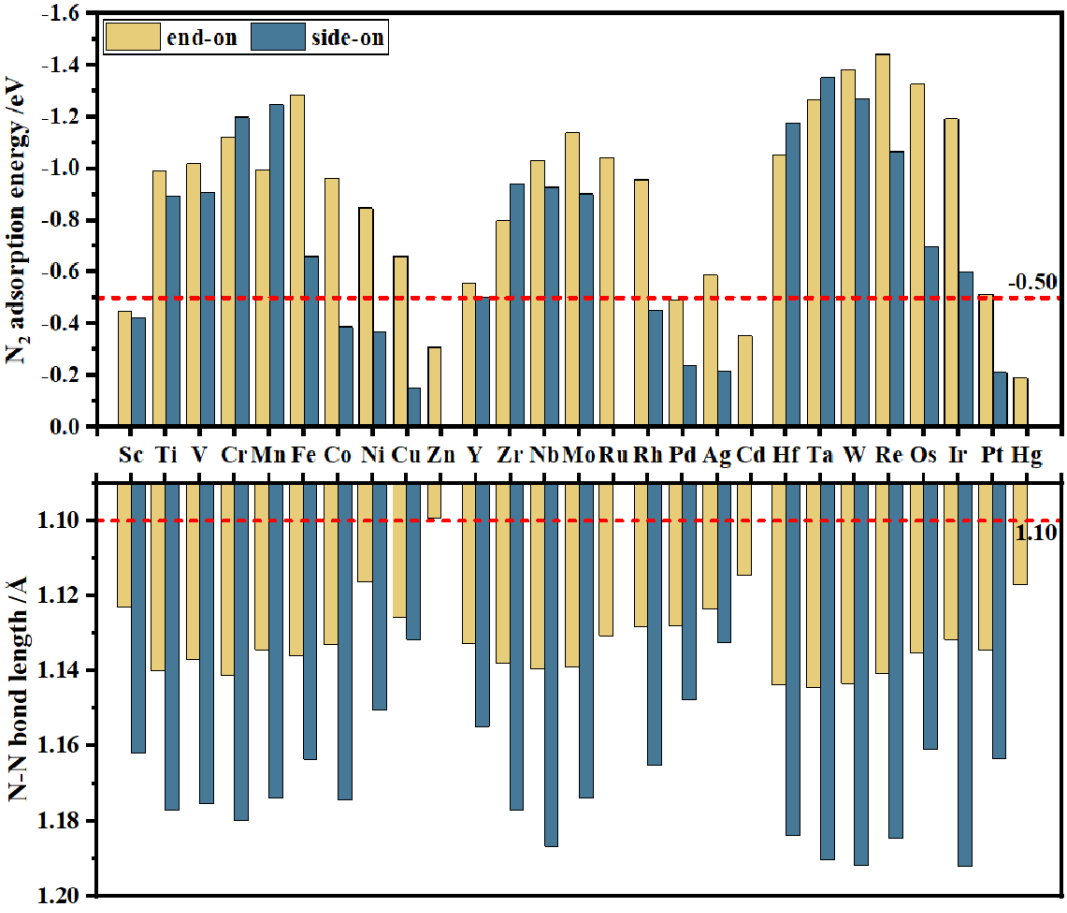

Figure 3. Adsorption energies (E_{ads}) and N-N bond lengths of N_2 adsorbed on TM@C_2N-NCM (TM = 3d, 4d, 5d transition metals) in end-on and side-on configurations. TM@C_2N-NCM:Transition metals into a two-dimensional C_2N-based nanomaterial.

activation (except for the Zn system, where minimal activation is observed). The side-on mode typically results in greater N_2 activation due to simultaneous interactions between both nitrogen atoms and the active metal center. To further elucidate the mechanism of N_2 activation at the metal active sites, Fe@C_2N-NCM and Nb@C_2N-NCM, which have been identified as the most promising NRR catalysts in subsequent studies, were selected for detailed analysis using charge density difference, Bader charge, and projected density of states (PDOS) calculations. In both systems, the N_2 molecules adopt the side-on configuration. As shown in Figure 4A and B, significant electron transfer occurs between the metal atoms and the adsorbed N_2 molecules, resulting in charge accumulation at the TM-N interface and depletion along the N≡N bond. This electron redistribution is consistent with the classical "donation-acceptance" mechanism, where the empty *d* orbitals of metal atoms accept electron density from the lone pairs of N_2, while simultaneously back-donating electrons from their *d* orbitals into the N_2 anti-bonding orbitals, thereby weakening the N≡N bond. This results in an N≡N bond elongation to 1.16 Å for Fe and 1.19 Å for Nb, compared to 1.10 Å for free N_2. Bader charge analysis further confirms this interaction, with Fe and Nb donating 0.37 e^- and 0.58 e^- to N_2, respectively. Additionally, PDOS analysis[Figure 4C and D] reveals significant overlap between the *d* orbitals of the TM atoms and the *2p* orbitals of N_2 near the Fermi level. This strong orbital hybridization reveals the robust interaction between the metal centers and the adsorbed N_2, which is crucial for efficient N_2 activation and subsequent hydrogenation steps required for NRR. Based on the first screening criteria, five metals (Sc, Zn, Pd, Cd, Hg) were excluded due to weak N_2 binding. The remaining 22 TMs (TM = Ti, V, Cr, Mn, Fe, Co, Ni, Cu, Y, Zr, Nb, Mo, Ru, Rh, Ag, Hf, Ta, W, Re, Os, Ir, Pt) correspond to 37 distinct N_2 adsorption systems, comprising 22 end-on and 15 side-on configurations.

Screening of the first and last protonation steps

After the initial screening based on N_2 adsorption, the ΔG values for the first and last protonation steps were calculated for 37 N_2 adsorption systems to refine the catalyst selection. As shown in Figure 5, eleven systems in the yellow-shaded region meet the second and third screening criteria ($\Delta G(*N_2 \rightarrow *NNH) < 0.55$ eV and $\Delta G(*NH_2 \rightarrow *NH_3) < 0.55$ eV). Of these, nine TM@C_2N-NCM systems (TM = Ti, V, Fe, Zr, Nb, Ta, W, Os, Ir) exhibit side-on N_2 adsorption; one (Pt@C_2N-NCM) shows end-on adsorption, and Mn@C_2N-NCM supports both adsorption modes. These eleven systems were the final candidates screened for comprehensive evaluation of their NRR catalytic performance. It should be noted that our earlier work involving analogous structures has shown that the impact of solvation on the ΔG of key reaction steps is within 0.15 eV[47]. Therefore, the solvation effect is not considered in this study.

Full reaction pathways and selectivity

U_L, which corresponds to the maximum free energy change (ΔG_{max}) in the PDS, is commonly used to evaluate the catalytic activity of NRR catalysts. To accurately determine U_L, full-pathway calculations were performed for the eleven systems identified in the screening process. For catalysts with side-on adsorption (TM = Ti, V, Fe, Zr, Nb, Ta, W, Os, Ir), both enzymatic and consecutive pathways were analyzed. The distal and alternating pathways were evaluated for the Pt system due to the end-on adsorption, while Mn, capable of both adsorption modes, was assessed across all four pathways. The U_L values and corresponding PDS for each system are illustrated in Figure 6A. The full reaction pathway for Nb@C_2N-NCM, which demonstrated the best catalytic performance, is presented in Figure 6B, while the pathways for the remaining systems are provided in Supplementary Figure 2. Generally, the protonation steps across all pathways exhibit a characteristic increasing-decreasing energy trend. Seven systems exhibit the PDS in the first protonation step, with corresponding U_L values of -0.46 V for V, -0.42 V for Mn, -0.30 V for Fe, -0.29 V for Nb, -0.47 V for Ta, -0.44 V for W, -0.53 V for Os, -0.51 V for Ir, and -0.44 V for Pt. Among these, Nb@C_2N-NCM demonstrated the lowest U_L, indicating the highest catalytic activity. In the cases of Zr@C_2N-NCM and Ta@C_2N-NCM, the PDS is located in the last step of the consecutive pathway, with U_L values of -0.48 V and -0.47 V, respectively. For Ti@C_2N-NCM, the PDS occurs during the third step of the enzymatic pathway

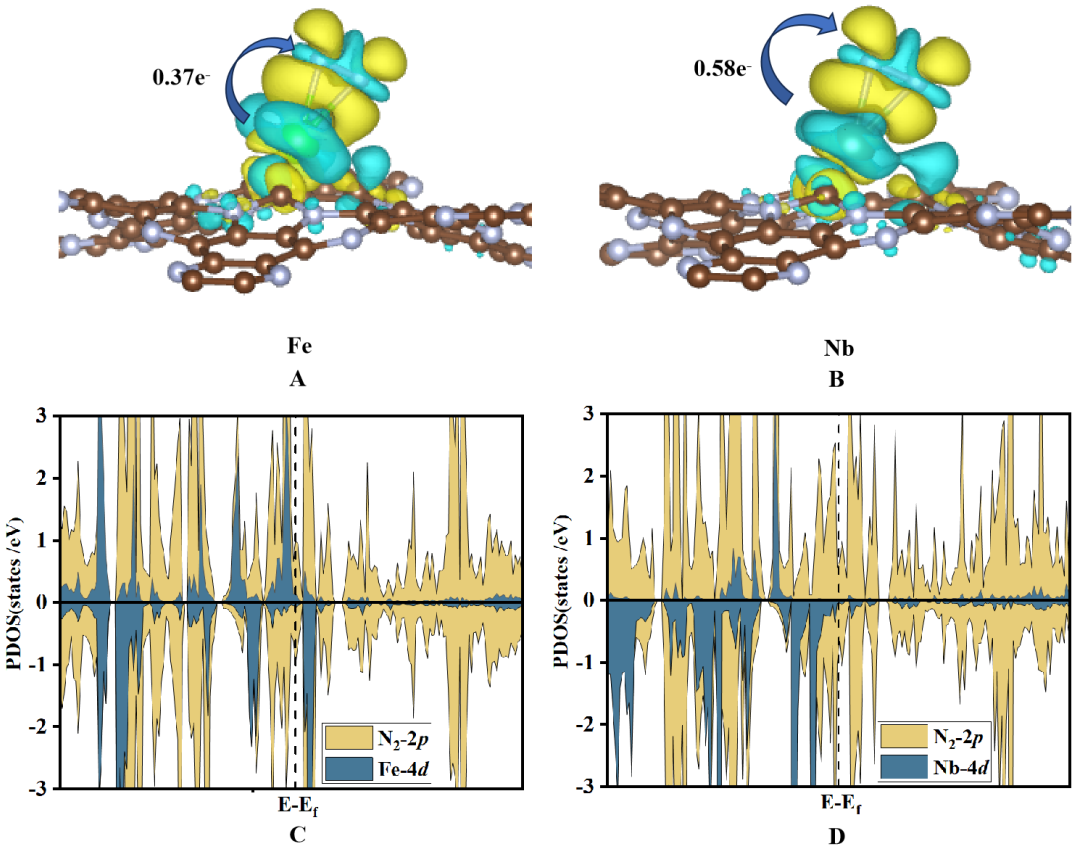

Figure 4. (A) The Charge density difference for Fe@C_2N-NCM and (B) Nb@C_2N-NCM, with yellow and blue regions representing electron accumulation and depletion, respectively. The isosurface level is set at 0.0003 e/Å^3; (C, D) PDOS for N_2 adsorption on Fe@C_2N-NCM and Nb@C_2N-NCM. NCM: N-heterocyclic carbene nanomaterial; PDOS: Projected density of states.

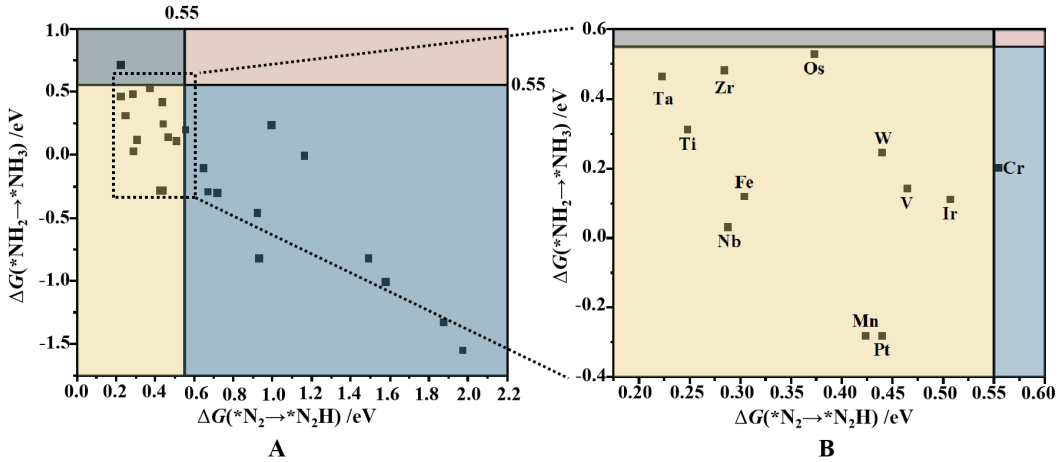

Figure 5. (A) Second and third step screening results of TM@C_2N-NCM, based on the ΔG for $*N_2 \rightarrow *NNH$ and $*NH_2 \rightarrow *NH_3$. The yellow-shaded region in the lower-left contains the materials that passed both criteria; (B) Close-up view of the yellow-shaded region. TM@C_2N-NCM: Transition metals into a two-dimensional C_2N-based nanomaterial.

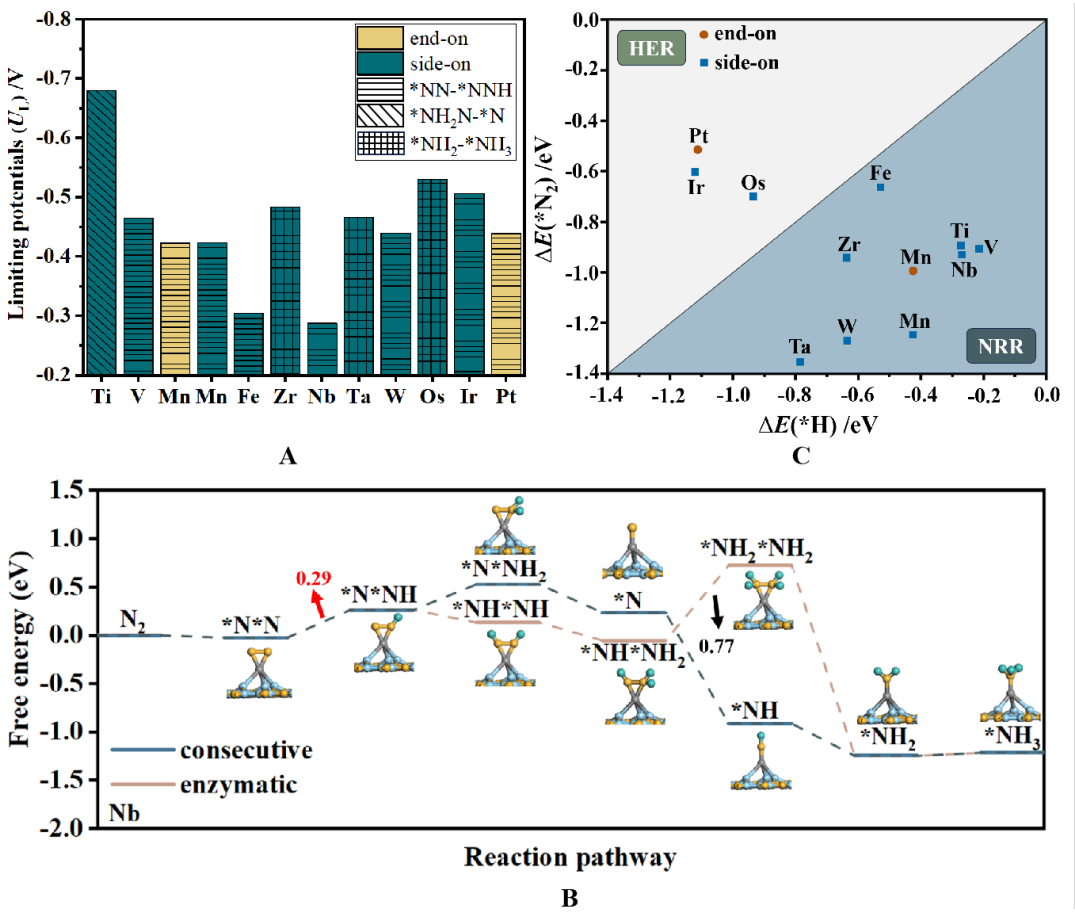

Figure 6. (A) Calculated theoretical U_L and corresponding PDS for 11 TM@C_2N-NCM catalysts. The color indicates the N_2 adsorption configuration, and the grid pattern represents the protonation step in which the PDS occurs; (B) Calculated free energy diagrams for NRR via the enzymatic and consecutive mechanisms on Nb@C_2N-NCM; (C) Comparison of adsorption energies (ΔE) for *N_2 and *H. TM@C_2N-NCM: Transition metals into a two-dimensional C_2N-based nanomaterial; PDS: Potential-determining steps; NCM: N-heterocyclic carbene nanomaterial; NRR: Nitrogen reduction reaction.

(*NH*NH + H^+ + e^- → *NH_2*NH), yielding a U_L of -0.68 V. Except for Ti, all systems follow the above-expected strategy, with the most significant energy barrier occurring in either the first or last protonation step, and the values are within the limits set by our screening criteria. Remarkably, compared to TM@graphene-NCM catalysts[47], the range of TMs that exhibit high catalytic performance in the screened TM@C_2N-NCM systems is broader. Moreover, the U_L values for all TM@C_2N-NCM systems are significantly lower, indicating enhanced catalytic activity. This demonstrates that the C_2N substrate plays a crucial role in optimizing the interaction between the active metal sites and N_2, leading to improved catalytic performance. Next, we evaluated the competition with the hydrogen evolution reaction (HER), a major side reaction in NRR, by comparing the E_{ads} of N_2 and H at the active sites (see Figure 6C). More negative E_{ads} values indicate a preference for adsorption at the active sites. Among the eleven systems, three (TM = Ir, Os, Pt) exhibit a stronger preference for H adsorption, suggesting lower selectivity for NRR. The remaining eight systems show more stable N_2 adsorption, demonstrating better selectivity for NRR. In summary, based on the systematic evaluation, eight TM@C_2N-NCM systems were finally identified as potential high-activity and high-selectivity NRR catalysts. The catalytic activity follows the order: Nb > Fe > Mn > W > Pt > V > Ta > Zr > Ir > Os > Ti.

Although the computational hydrogen electrode (CHE) model can effectively describe the reaction mechanism and catalytic activity of NRR on Nb@C_2N-NCM, it is overly simplistic for complex working conditions, considering the influence of electrode potential only through energy correction. Therefore, we further employed the Standard Hydrogen Electrode (SHE) model to investigate the effect of potential on the NRR activity of Nb@C_2N-NCM. Supplementary Figure 3A shows the computed energies as a function of the applied electrode potential (*vs.* SHE) for Nb@C_2N-NCM and the corresponding reaction intermediates. It demonstrates that the energy-potential points fit well into a quadratic function. As shown in Supplementary Figure 3B, we obtained the electrode potential-dependent free energy curves. The results indicate that Nb@C_2N-NCM exhibits the best catalytic activity at an electrode potential of -3V, with the corresponding U_L determined to be -0.14 V *vs.* SHE. Subsequently, we considered the effect of potential on the selectivity of the catalyst [Supplementary Figure 3C]. The results show that within the potential range considered, N_2 always has lower E_{ads} and more readily occupies the active sites of the catalyst compared to the H atom, indicating excellent selectivity for NRR over HER.

Machine learning analysis

To explore the intrinsic factors influencing the catalytic performance of NRR catalysts, ML was employed to uncover the relationships between fundamental physicochemical properties and catalytic activity. The workflow of the ML approach is shown in Figure 7. The target variable dataset was derived from the DFT-calculated results. Based on previous studies and validation in this work, the first and last protonation steps were identified as key steps for assessing catalyst activity. These steps are collectively referred to as Candidate Potential Determining Steps (C-PDS), and were used as the target variable for ML analysis. The final dataset includes 28 ΔG values for the end-on mode first protonation, 24 for the side-on mode first protonation, and 28 for the final protonation step.

To construct a reliable feature set, 20 features were selected (see Supplementary Table 2). Seventeen of these features represent the inherent properties of TM atoms, such as Pauling electronegativity (χ_P), the number of d-electrons (N_d), and electron affinity (EA), with values obtained from the National Institute of Standards and Technology (NIST) database[78].

Additionally, three binary features were introduced to distinguish between different protonation steps and adsorption modes: S_{1E} (first-step protonation of side-on adsorption), S_{1S} (first-step protonation of end-on adsorption), and S_6 (last-step protonation). These features were encoded as one-hot vectors and incorporated into the feature set. We first analyzed the Pearson correlation among the 20 features to identify any potential redundancy. Subsequently, the RFE method was employed to select the optimal feature subset. The Pearson correlation heatmap is presented in Supplementary Figure 4, while the final dataset after feature selection is summarized in Supplementary Table 3. The results of optimal ML models using three algorithms (XGBR, GBR, RFR) are shown in Figure 8A-C. All models demonstrated strong linear correlations between the predicted values and the DFT-calculated results, with R^2 values ranging from 0.88 to 0.91 and MAE values between 0.19 and 0.24, indicating excellent predictive performance across all models. Among these, XGBR exhibited the best performance, achieving the highest R^2 and the lowest MAE. Additionally, the average R^2 and MAE values from the 5-fold cross-validation are summarized in Figure 8D, further confirming XGBR as the best-performing model. Furthermore, we conducted additional model training using eight features for comparison. The results, as shown in Supplementary Figure 5, indicate that the average scores are very close, thereby supporting the reliability of the model.

Feature importance analysis revealed that the one-hot encoded features S_6 contributed the most, accounting for 56.96% of the total importance. These features are crucial for distinguishing between the first and last

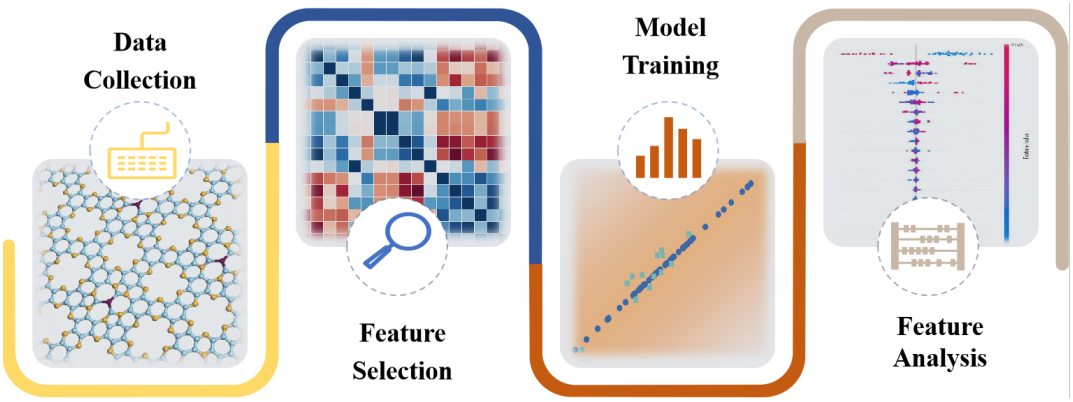

Figure 7. Workflow of the machine learning approach.

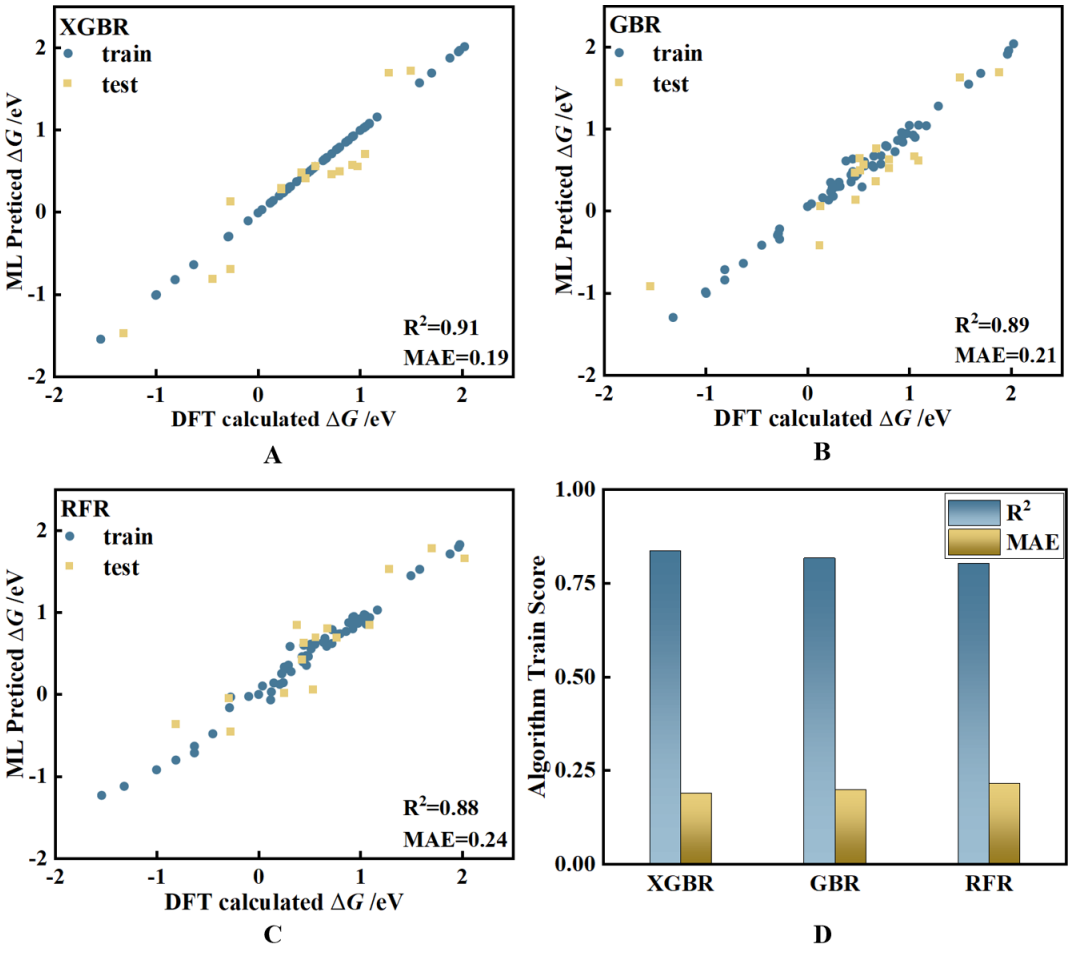

Figure 8. (A-C) Comparison of DFT-calculated ΔG values with those predicted by three ML algorithms; (D) Average R^2 and MAE scores from 5-fold cross-validation for three ML models. DFT: Density functional theory; ML: Machine learning; MAE: Mean absolute error.

protonation steps, and identifying the side-on and end-on adsorption modes in the first protonation step. The Mendeleev number (N_m) and N_d of the metal atom ranked as the second and third most important features, contributing 23.77% and 8.94%, respectively (see Figure 9A). This indicates that these two intrinsic

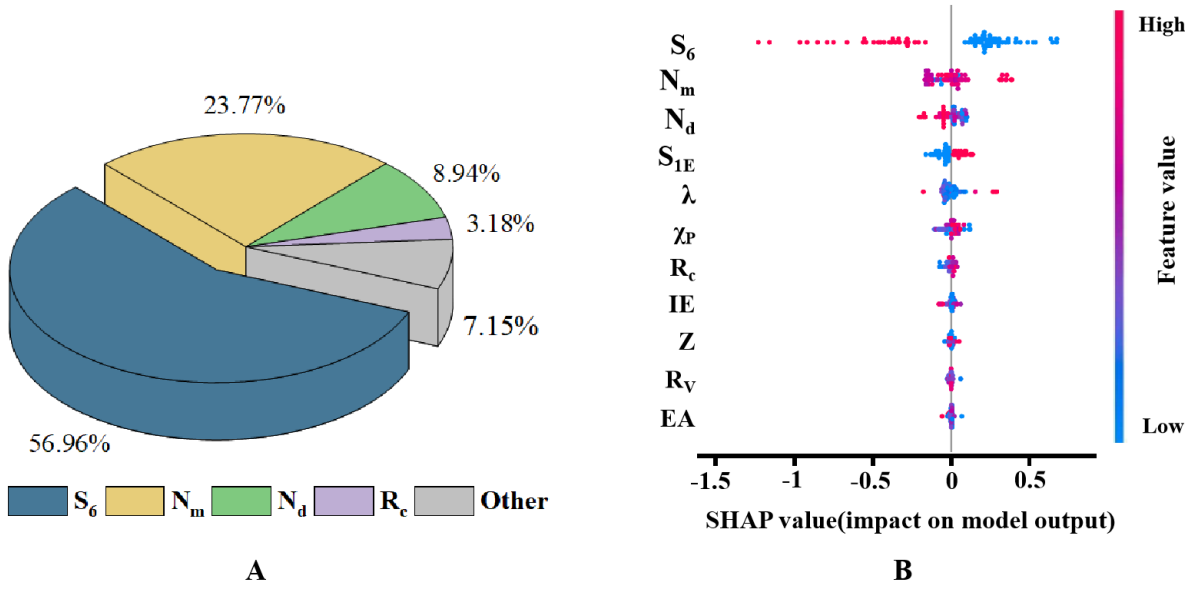

Figure 9. (A) Feature importance and (B) SHAP value distribution in XGBR model. SHAP: Shapley additive explanations; XGBR: Extreme gradient boosting regression.

properties of the metal center play a key role in determining the catalytic performance of the catalysts. To further understand the relationships between C-PDS and the key features, SHAP analysis was employed. As shown in Figure 9B, the most important feature S_6 has a clear bipolar distribution, indicating that the last protonation step generally has a lower ΔG than the first step. Similarly, S_{1E}, ranked fourth, reveals that end-on adsorption tends to result in a higher energy barrier for the first protonation step. N_m, the second most important feature, showed a more complex SHAP distribution, reflecting its multidimensional nature. As an ordering system for chemical elements, N_m incorporates various elemental properties such as electron configuration, atomic radius, and ionization energy, leading to a mixture of SHAP values. Nevertheless, N_m plays a significant role in influencing catalytic activity, consistent with previous findings on TM@graphene-NCM. The third most important feature, N_d, also showed a clear correlation with C-PDS. Higher N_d values tend to lower the C-PDS, suggesting that a greater N_d enhances the interaction between the TM center and N_2, promoting N_2 activation and reducing the reaction barrier. These findings provide valuable insights into the factors influencing NRR activity in TM@C_2N-NCM systems and offer guidance for the design and optimization of carbene-coordinated SACs based on the identified universal principles.

CONCLUSIONS

In this study, a combination of DFT calculations and ML methods was employed to comprehensively evaluate the NRR catalytic performance of 28 TM@C_2N-NCM catalysts by embedding TMs into a two-dimensional C_2N-NCM substrate. Through multi-step screening, full-pathway validation, and competition analysis with HER, eight catalysts (TM = Nb, Fe, Mn, W, V, Ta, Zr, Ti) with high activity and selectivity were identified. Among them, Nb@C_2N-NCM exhibited the best performance, with U_L of -0.29 V . Remarkably, all identified catalysts showed lower U_L values than their TM@graphene-NCM counterparts, revealing the crucial role of the C_2N substrate in enhancing catalytic performance. ML analysis using the XGBR achieved excellent predictive accuracy for C-PDS free energies, with an R^2 of 0.91 and MAE of 0.19. Feature importance analysis identified S_6, N_m, and N_d as the most influential factors affecting NRR catalytic performance. SHAP analysis further validated the significant roles of these features, demonstrating that tuning these intrinsic properties can effectively modulate the catalytic activity of TM@C_2N-NCM catalysts.

This study demonstrates that combining C_2N substrates with NHC coordination can significantly enhance the performance of SACs for NRR. The findings provide universal guidelines for understanding NHC-coordinated SACs and offer new insights into the rational design of high-performance NRR catalysts.

DECLARATIONS

Authors' contributions

Made substantial contributions to the conception and design of this article, writing, and editing: Lu W, Xu J, Liu W

Assisted in processing the data of DFT calculations: Lu W, Zheng D

Provided technical support for machine learning and completed analysis and processing of data: Zheng D, Ye D

Performed data acquisition and interpretation: Lu W, Zheng D, Peng J, Gong X

Provided guidance and revised the manuscript: Xu J, Liu W

Availability of data and materials

The rata data supporting the findings of this study are available within this article and its Supplementary Materials. Further data are available from the corresponding authors upon request.

Financial support and sponsorship

This work is supported by the National Natural Science Foundation of China (No.12075211) and the Scientific Research Foundation of Zhejiang A&F University (No.2019FR005).

Conflicts of interest

All authors declared that there are no conflicts of interest.

Ethical approval and consent to participate

Not applicable.

Consent for publication

Not applicable.

REFERENCES

1. Canfield DE, Glazer AN, Falkowski PG. The evolution and future of Earth's nitrogen cycle. *Science* 2010;330:192-6. DOI PubMed
2. Foster SL, Bakovic SIP, Duda RD, et al. Catalysts for nitrogen reduction to ammonia. *Nat Catal* 2018;1:490-500. DOI
3. Rosca V, Duca M, de Groot MT, Koper MT. Nitrogen cycle electrocatalysis. *Chem Rev* 2009;109:2209-44. DOI PubMed
4. Liu H. Ammonia synthesis catalyst 100 years: Practice, enlightenment and challenge. *Chin J Catal* 2014;35:1619-40. DOI
5. Lehnert N, Musselman BW, Seefeldt LC. Grand challenges in the nitrogen cycle. *Chem Soc Rev* 2021;50:3640-6. DOI PubMed
6. Smil V. Detonator of the population explosion. *Nature* 1999;400:415-415. DOI
7. Kyriakou V, Garagounis I, Vourros A, Vasileiou E, Stoukides M. An electrochemical haber-bosch process. *Joule* 2020;4:142-58. DOI
8. Chen JG, Crooks RM, Seefeldt LC, et al. Beyond fossil fuel-driven nitrogen transformations. *Science* 2018;360:eaar6611. DOI
9. Yu L, Li F. Pt_2 dimer anchored vertically in defective BN monolayer as an efficient catalyst for N_2 reduction: a DFT Study. *Catalysts* 2022;12:1387. DOI
10. Zhao X, Zhang X, Xue Z, Chen W, Zhou Z, Mu T. Fe nanodot-decorated MoS_2 nanosheets on carbon cloth: an efficient and flexible electrode for ambient ammonia synthesis. *J Mater Chem A* 2019;7:27417-22. DOI
11. Li S, Peng M, Song Y, et al. Screening transition metal and nonmetal atoms co-doped graphyne as efficient single-atom catalysts for nitrogen reduction. *Chem Eng J* 2024;495:153275. DOI
12. Wang S, Shi L, Bai X, Li Q, Ling C, Wang J. Highly efficient photo-/electrocatalytic reduction of nitrogen into ammonia by dual-metal sites. *ACS Cent Sci* 2020;6:1762-71. DOI PubMed PMC

13. Yang X, Shang C, Zhou S, Zhao J. MBenes: emerging 2D materials as efficient electrocatalysts for the nitrogen reduction reaction. *Nanoscale Horiz* 2020;5:1106-15. DOI
14. Han B, Li F. Regulating the electrocatalytic performance for nitrogen reduction reaction by tuning the N contents in Fe_3@N*x*C_{20-x} (*x* = 0~4): a DFT exploration. *J Mater Inf* 2023;3:24. DOI
15. Cao J, Hu Y, Zheng Y, Zhang W, Yu B. Recent advances and challenges of nitrogen/nitrate electro catalytic reduction to ammonia synthesis. *Front Energy* 2024;18:128-40. DOI
16. Ren Y, Yu C, Tan X, Huang H, Wei Q, Qiu J. Strategies to suppress hydrogen evolution for highly selective electrocatalytic nitrogen reduction: challenges and perspectives. *Energy Environ Sci* 2021;14:1176-93. DOI
17. Cui Y, Ren C, Li Q, Ling C, Wang J. Hybridization state transition under working conditions: activity origin of single-atom catalysts. *J Am Chem Soc* 2024;146:15640-7. DOI
18. Liu T, Jing Y, Li Y. First-principles insights into the selectivity of CO_2 electroreduction over heterogeneous single-atom catalysts. *J Phys Chem Lett* 2024;15:6216-21. DOI
19. Sun H, Liu J. Advancing CO_2RR with O-coordinated single-atom nanozymes: a DFT and machine learning exploration. *ACS Catal* 2024;14:14021-30. DOI
20. Liu S, Xing G, Liu J. Computational screening of single-atom catalysts for direct electrochemical NH_3 synthesis from NO on defective boron phosphide monolayer. *Appl Surf Sci* 2023;611:155764. DOI
21. Wang Q, Yu G, Yang E, Chen W. Through the self-optimization process to achieve high OER activity of SAC catalysts within the framework of TMO_3@G and TMO_4@G: a high-throughput theoretical study. *J Colloid Interface Sci* 2023;640:405-14. DOI
22. Guo W, Wang S, Wang H, Cai Q, Zhao J. Cooperation between single atom catalyst and support to promote nitrogen electroreduction to ammonia: a theoretical insight. *J Energy Chem* 2024;96:336-44. DOI
23. Yin Z, Li Y, Ye Y, et al. Sp/sp^2 carbon ratio-driven high-throughput screening of electrocatalytic nitrogen reduction performance on transition metal single-atom catalysts. *Rare Met* 2024;43:5781-91. DOI
24. Zhang Y, Wang X, Liu T, et al. Charge and spin communication between dual metal single-atom sites on C_2N sheets: regulating electronic spin moments of Fe atoms for N_2 activation and reduction. *J Mater Chem A* 2022;10:23704-11. DOI
25. Liu J, Cai Y, Song R, et al. Recent progress on single-atom catalysts for CO_2 electroreduction. *Mater Today* 2021;48:95-114. DOI
26. Iqbal S, Safdar B, Hussain I, Zhang K, Chatzichristodoulou C. Trends and prospects of bulk and single-atom catalysts for the oxygen evolution reaction. *Adv Energy Mater* 2023;13:2203913. DOI
27. Song W, Xiao C, Ding J, et al. Review of carbon support coordination environments for single metal atom electrocatalysts (SACS). *Adv Mater* 2024;36:e2301477. DOI
28. Shen Y, Liang L, Zhang S, et al. Organelle-targeting surface-enhanced raman scattering (SERS) nanosensors for subcellular pH sensing. *Nanoscale* 2018;10:1622-30. DOI
29. Liu S, Liu J. Rational design of highly efficient electrocatalytic single-atom catalysts for nitrogen reduction on nitrogen-doped graphene and g-C_2N supports. *J Power Sources* 2022;535:231449. DOI
30. Jiao D, Liu Y, Cai Q, Zhao J. Coordination tunes the activity and selectivity of the nitrogen reduction reaction on single-atom iron catalysts: a computational study. *J Mater Chem A* 2021;9:1240-51. DOI
31. Long X, Huang F, Yao Z, et al. Advancements in electrocatalytic nitrogen reduction: a comprehensive review of single-atom catalysts for sustainable ammonia synthesis. *Small* 2024;20:e2400551. DOI
32. Dai E, An W, Guo R, et al. Two-dimensional C_2N-based single-atom catalyst with complex microenvironment for enhanced electrochemical nitrogen reduction: a descriptor-based design. *J Energy Chem* 2024;97:110-9. DOI
33. Xu M, Ji Y, Qin Y, Dong H, Li Y. A universal descriptor for two-dimensional carbon nitride-based single-atom electrocatalysts towards the nitrogen reduction reaction. *J Mater Chem A* 2024;12:28046-55. DOI
34. Liu Y, Zhao Z, Wei W, et al. Single-atom Fe-N_4 on a carbon substrate for nitrogen reduction reaction. *ACS Appl Nano Mater* 2021;4:13001-9. DOI
35. Shen P, Li X, Luo Y, Zhang N, Zhao X, Chu K. Ultra-efficient N_2 electroreduction achieved over a rhodium single-atom catalyst (Rh_1/MnO_2) in water-in-salt electrolyte. *Appl Catal B: Environ* 2022;316:121651. DOI
36. Feng X, Liu J, Chen L, et al. Hydrogen radical-induced electrocatalytic N_2 reduction at a low potential. *J Am Chem Soc* 2023;145:10259-67. DOI
37. Geng Z, Liu Y, Kong X, et al. Achieving a Record-High Yield Rate of 120.9 $\mu g_{NH_3}\ mg_{cat.}^{-1}\ h^{-1}$ for N_2 electrochemical reduction over Ru single-atom Catalysts. *Adv Mater* 2018;30:e1803498. DOI
38. Ling C, Ouyang Y, Li Q, et al. A general two-step strategy-based high-throughput screening of single atom catalysts for nitrogen fixation. *Small Methods* 2019;3:1800376. DOI
39. Choi CH, Kim M, Kwon HC, et al. Tuning selectivity of electrochemical reactions by atomically dispersed platinum catalyst. *Nat Commun* 2016;7:10922. DOI PubMed PMC
40. Liu C, Cui Y, Zhou Y. The recent progress of single-atom catalysts on amorphous substrates for electrocatalysis. *Energy Mater* 2024;4:400067. DOI
41. Yang X, Wan J, Zhang H, Wang Y. In situ modification of the d-band in the core-shell structure for efficient hydrogen storage via electrocatalytic N_2 fixation. *Chem Sci* 2022;13:11030-7. DOI
42. Liu X, Qi L, Song E, Gao W. Effective descriptor for nitrogen reduction on atomic catalysts. *Catal Lett* 2023;153:300-10. DOI
43. Cui X, Wang X, Fu C, et al. Tuning the local coordination environment of silver(I) coordination networks with counterions for

enhanced electrocatalytic CO_2 reduction. *Sci China Chem* 2024;67:1524-30. DOI
44. Sun Y, Fan W, Li Y, et al. Tuning coordination structures of Zn sites through symmetry-breaking accelerates electrocatalysis. *Adv Mater* 2024;36:e2306687. DOI
45. Liu W, Liu S, Guo K, et al. Low-dimensional N-heterocyclic carbenes nanomaterials: promising supports of single atom catalysts. *Vacuum* 2024;227:113390. DOI
46. Liu W, Xie Y, Tong Z, Sun J, Chen L, Xu J. Heterogeneous N-heterocyclic carbenes: efficient and selective metal-free electrocatalysts for CO reduction to multi-carbon products. *J CO2 Util* 2023;75:102566. DOI
47. Sun J, Zheng D, Deng F, et al. Heterogeneous N-heterocyclic carbenes supported single-atom catalysts for nitrogen fixation: a combined density functional theory and machine learning study. *Appl Surf Sci* 2024;644:158802. DOI
48. Liu W, Xie Y, Peng J, Zheng D, Lu W, Xu J. Synergistic N-heterocyclic carbene and C_2N integration for efficient and selective metal-free photocatalytic CO reduction to C_2H_5OH. *Appl Surf Sci* 2024;678:161122. DOI
49. Liu W, Sun J, Xie Y, Chen L, Xu J. The effective regulation of heterogeneous N-heterocyclic carbenes: structures, electronic properties and transition metal adsorption. *Phys Chem Chem Phys* 2023;25:28382-92. DOI
50. Miller TS, Jorge AB, Suter TM, Sella A, Corà F, McMillan PF. Carbon nitrides: synthesis and characterization of a new class of functional materials. *Phys Chem Chem Phys* 2017;19:15613-38. DOI PubMed
51. Longuinhos R, Ribeiro-soares J. Stable holey two-dimensional C_2N structures with tunable electronic structure. *Phys Rev B* 2018:97. DOI
52. Wei Z, He J, Yang Y, Xia Z, Feng Y, Ma J. Fe, V-co-doped C_2N for electrocatalytic N_2-to-NH_3 conversion. *J Energy Chem* 2021;53:303-8. DOI
53. Li Y, Yang T, Wang S, Bian Z, Liu Z. A recyclable Cu@C_2N nano-catalyst applied in the transformation of alkynes: pH switchable access to ketones and 1,3-diynes. *Green Chem* 2024;26:2540-5. DOI
54. Kresse G, Furthmüller J. Efficiency of ab-initio total energy calculations for metals and semiconductors using a plane-wave basis set. *Comput Mater Sci* 1996;6:15-50. DOI
55. Blöchl PE. Projector augmented-wave method. *Phys Rev B Condens Matter* 1994;50:17953-79. DOI PubMed
56. Hammer B, Hansen LB, Nørskov JK. Improved adsorption energetics within density-functional theory using revised perdew-burke-ernzerhof functionals. *Phys Rev B* 1999;59:7413-21. DOI
57. Chadi DJ. Special points for brillouin-zone integrations. *Phys Rev B* 1977;16:1746-7. DOI
58. Bussi G, Donadio D, Parrinello M. Canonical sampling through velocity rescaling. *J Chem Phys* 2007;126:014101. DOI PubMed
59. Grimme S, Antony J, Ehrlich S, Krieg H. A consistent and accurate ab initio parametrization of density functional dispersion correction (DFT-D) for the 94 elements H-Pu. *J Chem Phys* 2010;132:154104. DOI PubMed
60. Bader RFW. A quantum theory of molecular structure and its applications. *Chem Rev* 1991;91:893-928. DOI
61. Sahour H, Gholami V, Torkaman J, Vazifedan M, Saeedi S. Random forest and extreme gradient boosting algorithms for streamflow modeling using vessel features and tree-rings. *Environ Earth Sci* 2021;80:10054. DOI
62. Umer M, Umer S, Zafari M, et al. Machine learning assisted high-throughput screening of transition metal single atom based superb hydrogen evolution electrocatalysts. *J Mater Chem A* 2022;10:6679-89. DOI
63. Tamtaji M, Gao H, Hossain MD, et al. Machine learning for design principles for single atom catalysts towards electrochemical reactions. *J Mater Chem A* 2022;10:15309-31. DOI
64. Ding R, Wang R, Ding Y, et al. Designing AI-aided analysis and prediction models for nonprecious metal electrocatalyst-based proton-exchange membrane fuel cells. *Angew Chem Int Ed Engl* 2020;59:19175-83. DOI
65. Naceur H, Abdo HG, Igmoullan B, Namous M, Alshehri F, A Albanai J. Implementation of random forest, adaptive boosting, and gradient boosting decision trees algorithms for gully erosion susceptibility mapping using remote sensing and GIS. *Environ Earth Sci* 2024;83:11424. DOI
66. Ali Y, Awwad E, Al-razgan M, Maarouf A. Hyperparameter search for machine learning algorithms for optimizing the computational complexity. *Processes* 2023;11:349. DOI
67. Bischl B, Binder M, Lang M, et al. Hyperparameter optimization: Foundations, algorithms, best practices, and open challenges. *WIREs Data Min Knowl* 2023;13:e1484. DOI
68. Pedregosa F, Varoquaux G, Gramfort A, et al. Scikit-learn: machine learning in python. *J Mach Learn Res* 2011;12:2825-30. Available from: https://dl.acm.org/doi/10.5555/1953048.2078195. [Last accessed on 28 Dec 2024].
69. Guyon I, Elisseeff A. An introduction to variable and feature selection. *J Mach Learn Res* 2003;3:1157-82. DOI
70. Aas K, Jullum M, Løland A. Explaining individual predictions when features are dependent: more accurate approximations to shapley values. *Artif Intell* 2021;298:103502. DOI
71. Lv X, Wei W, Huang B, Dai Y, Frauenheim T. High-throughput screening of synergistic transition metal dual-atom catalysts for efficient nitrogen fixation. *Nano Lett* 2021;21:1871-8. DOI
72. Xiao Y, Shen C, Long T. Theoretical establishment and screening of an efficient catalyst for N_2 electroreduction on two-dimensional transition-metal borides (MBenes). *Chem Mater* 2021;33:4023-34. DOI
73. Seh ZW, Kibsgaard J, Dickens CF, Chorkendorff I, Nørskov JK, Jaramillo TF. Combining theory and experiment in electrocatalysis: Insights into materials design. *Science* 2017;355:eaad4998. DOI PubMed
74. Lv SY, Huang CX, Li G, Yang LM. Electrocatalytic mechanism of N_2 reduction reaction by single-atom catalyst rectangular TM-TCNQ monolayers. *ACS Appl Mater Interfaces* 2021;13:29641-53. DOI

75. Liu L, Yang L, Zhang H, et al. Screening strategies for diatom metal-doped β-borophene nanosheet catalysts for electrochemical synthesis of ammonia using density functional theory. *Energy Fuels* 2023;37:9682-91. DOI
76. Yue Y, Chen Y, Zhang X, Qin J, Zhang X, Liu R. High-throughput screening of highly active and selective single-atom catalysts for ammonia synthesis on WB_2 (001) surface. *Appl Surf Sci* 2022;606:154935. DOI
77. Pei W, Zhang W, Yu X, et al. Computational design of spatially confined triatomic catalysts for nitrogen reduction reaction. *J Mater Inf* 2023;3:26. DOI
78. NIST Chemistry WebBook. NIST Standard Reference Database Number 69. Available from: https://doi.org/10.18434/T4D303. [Last accessed on 22 Dec 2024].